Journal of Physics and Chemistry of Solids 182 (2023) 111597

Contents lists available at ScienceDirect

Journal of Physics and Chemistry of Solids

journal homepage: www.elsevier.com/locate/jpcs

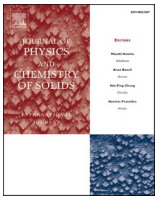

A novel Pt-free counter electrode based on $MoSe_2$ for cost effective dye-sensitized solar cells (DSSCs): Effect of Ni doping

Raed H. Althomali [a,*], Sulieman Ibraheem Shelash Al-Hawary [b], Anita Gehlot [c], Maytham T. Qasim [d], Barno Abdullaeva [e], I.B. Sapaev [f,g], Ibrahim H. Al-Kharsan [h], Ali Alsalamy [i]

[a] Department of Chemistry, Prince Sattam Bin Abdulaziz University, College of Arts and Science, Wadi Al-Dawasir, 11991, Saudi Arabia
[b] Department of Business Administration, Business School, Al al-Bayt University, P.O.BOX 130040, Mafraq, 25113, Jordan
[c] Department of Electronics and Communication Engineering, Uttaranchal Institute of Technology, Uttaranchal University, Dehradun, 248007, India
[d] Department of Anesthesia, College of Health and Medical Technology, Al-Ayen University, Thi-Qar, Iraq
[e] Tashkent State Pedagogical University, Tashkent, Uzbekistan
[f] Tashkent Institute of Irrigation and Agricultural Mechanization Engineers, National Research University, Tashkent, Uzbekistan
[g] New Uzbekistan University, Tashkent, Uzbekistan
[h] Computer Technical Engineering Department, College of Technical Engineering, The Islamic University, Najaf, Iraq
[i] College of Technical Engineering, Imam Ja'afar Al-Sadiq University, Al-Muthanna, 66002, Iraq

ARTICLE INFO

Keywords:
Dye-sensitized solar cell
Counter electrode
$MoSe_2$
Electrocatalytic behavior

ABSTRACT

In this study, we propose a new counter electrode based on the Ni-doped $MoSe_2$ as a viable counter electrode for DSSC applications. We investigate different ratios of Ni dopant inside the $MoSe_2$ lattice. Our results show that the introduction Ni can increase the active surface area and improve the electrocatalytic behavior of the $MoSe_2$ materials. We employed our prepared materials as the counter electrode in DSSCs and show that our optimized case demonstrates an open circuit voltage of 688 mV, a short circuit current density of 16 mA/cm^2, a fill factor of 63% resulting an efficiency of 6.94% which is a significant improvement from the 6.68% efficiency of the DSSCs fabricated from the high-cost platinum counter electrode.

1. Introduction

The future of energy market is moving toward the renewable energies with a fast pace and solar cells will play a significant role as clean and low-cost electrical power supplies [1,2]. Dye sensitized solar cells (DSSCs) are among the third-generation solar cells with huge potentials for future applications [3,4]. Unfortunately, the current share of DSSCs in harvesting the solar energy is so low and further research is required to bring DSSCs in to practical applications [5,6]. One factor that limits the effective use of DSSC, is the expensive price of its components and especially its counter electrode [7,8]. In DSSCs, the counter electrode is responsible for transferring electrons from the external circuit to the electrolyte and catalyzing the reduction of I_3^- to I^- in the electrolyte [9,10]. The conventional counter electrode is a fluorine-doped tin oxide (FTO) glass coated with a platinum electrocatalyst, which contributes to a major share of the cost of preparation due the use of expensive platinum element. Replacing this element with another high performance and lower cost electrocatalytic materials, can create new opportunities in the field of DSSCs [11,12]. Many attempts have been made to find an alternative material for platinum as the DSSC counter electrode. Electrocatalytic materials such as metal oxides [13,14], conductive polymers [15,16], nitrides [17,18], sulfides [19–21], carbides [22], carbon nanostructures [23,24], and 2D materials [25–28] have been investigated for this purpose with different ratios of success. Yet, more research is required to find a practical counter electrode material for DSSCs.

Recently, selenide materials have demonstrated outstanding performance in solar cells and photocatalyst materials. Zatirostami et al. showed that SnSe can be employed as the counter electrode material in DSSC and achieve comparable efficiencies to that of the platinum counter electrodes [29,30]. $MoSe_2$ is another selenide material with a narrow bandgap and lamellar crystal structure which huge potentials for DSSC applications [31,32]. Chen et al. employed an $MoSe_2$/Mo structure as the counter electrode and attained high efficiencies in DSSCs [33]. Lynch et al. demonstrated that $MoSe_2$/Graphene nanosheets as the DSSC's counter electrode can result in efficiencies up to 95% of the platinum counter electrode [34,35]. Furthermore, tapa et al. provided

* Corresponding author.
E-mail address: r.althomali@psau.edu.sa (R.H. Althomali).

https://doi.org/10.1016/j.jpcs.2023.111597
Received 15 June 2023; Received in revised form 28 July 2023; Accepted 29 July 2023
Available online 29 July 2023
0022-3697/© 2023 Published by Elsevier Ltd.

the guidelines and potentials for further development of metal chalcogenides counter electrodes [36]. Yet, this material requires more research and optimization to reach its potentials in solar cells.

In this study, we have employed the excellent electrochemical and electrocatalytic properties of $MoSe_2$ as a potential counter electrode for DSSCs. To further improve these properties, for the first time up to our best knowledge, we have used the Ni as a dopant to tune the properties of $MoSe_2$ according to DSSC requirements and demonstrated its capability as a replacement for conventional Pt counter electrodes. We attempt to further improve the $MoSe_2$ properties to increase its electrocatalytic and transport properties and thus making it more suitable for counter electrode employment. For this purpose, we introduce different ratios of Ni into its lattice structure. Yet, this method has not been tested for the counter electrodes of the DSSCs. The increased electrocatalytic behavior is very desirable for this purpose and we investigate different ratios of Ni dopant in $MoSe_2$ materials to achieve the optimized result. We believe that our new proposed counter electrode possesses enough potentials to replace platinum in DSSCs as a lower cost material and further increase the DSSCs feasibility.

2. Experimental method

2.1. Photoanode preparation

We employed FTO-coated glass with 2 × 1.5 cm size (15 Ω/□) as substrates and washed them using deionized water and ethanol solution. For further cleaning and removing any organics from the substrates, they were placed in an ultrasonic bath with acetone solvent and a temperature of 60 °C for 30 min. We deposited a 100 nm thin layer of TiO_2 on the FTOs using the RF sputtering method to act as a blocking layer. We acquired P25 standard TiO_2 nanoparticles from Merck Co and deposited them on the FTO substrates using the doctor blade technique. For this purpose, 100 mg of the TiO_2 nanoparticles were added to 5 mL HPLC Merck Co ethanol and stirred them for ~1 h so that a homogenous solution was acquired. In this step, we added a 0.1 g ethylene cellulose to the solution and continued stirring for another 1 h to attain a milky color solution. We also added 0.5 mL α-Terpineol and 6 drops of triton-X100 and increased the temperature of the solution to 80 °C. The stirring was continued for another 1 h so that a suitable and adhesive paste was acquired for deposition. The paste was cooled down to room temperature and doctor bladed on FTO substrates. The deposited layers were aged for 30 min and then transferred to an air furnace in which it was held at 500 °C for 45 min. This heat-treatment facilitates the evaporation of the organic materials from the layers and provides us with a mesoporous TiO_2 layer [37]. The layers were later cooled down to room temperature and placed in a 0.3 mM N719 dye (ethanol + acetonitrile) solution for 24 h for dye-sensitization.

2.2. $MoSe_2$:Ni counter electrode preparation

For preparation of the Ni-doped $MoSe_2$ counter electrodes, we also used ultrasonically cleaned FTO-coated glass substrates that were used as the working electrode in a three-electrode electrochemical cell. In this configuration, the counter electrode is a platinum wafer and an Ag/AgCl standard electrode plays the role of the reference electrode. Furthermore, the electrolyte is composed of 9.12 g Molybdic acid (H_2MoO_4, Merck Co) in 100 mL of 1.5 M ammoniacal solution (NH_3, Sigma Aldrich 99.98%) and 15 mg selenium dioxide (SeO_2, Merck Co, 99.9%) in 100 mL deionized water and different ratios (0, 36, 72 and 108 mg) of nickel (II) chloride ($NiCl_2$ Sigma-Aldrich 99.99%). The electrochemical deposition was conducted at 40 °C temperature for 10 min at working electrode potential of −1.10 V to achieve the required thickness of $MoSe_2$ thin films. We named the prepared counter electrodes according to the $NiCl_2$ quantities of 0, 36, 72 and 108 mg as Ni0, Ni1, Ni2 and Ni3 respectively. Moreover, we employed a standard platinum counter electrode in solar cell fabrication as the control sample to compare with our prepared counter electrodes.

2.3. Solar cell fabrication

After the preparation of the photoanode and counter electrodes, we fabricated our DSSCs. For this purpose, Surlyn spacers were sandwiched between the two electrodes which were placed with a small displacement from each other for installation of electrical contacts. We injected the iodide-tri-iodide electrolyte containing 0.05 M iodine, 0.5 M tert-butylpyridine, and 0.1 M lithium iodide, 0.1 M potassium iodide, 0.1 M sodium iodide through a micrometric drilled hole on the counter electrode which were later covered with Surlyn. The complete DSSC structures were sealed by adhesive epoxy. In order to minimize the characterization errors, we fabricated 20 DSSCs from each sample and reported their average results.

2.4. Characterization

We used an STOE STADI-P X-ray diffractometer (XRD) in the range of 2θ = 20 to 80 to analyze the crystalline structure of the samples. In order to acquire the morphological properties of the samples, we employed a Mira III Tescan field emission electron microscope (FESEM) with 15 kV operating voltage. The optical and bandgap analysis of the prepared materials were carried out by a 3648 Avantes UV–visible spectrometer in the wavelength range of 300–800 nm. To investigate the electrocatalytic behavior of the CEs, we used a high end, high current potentiostat/galvanostat (AUTOLAB 302 N). The porosity of the CEs was analyzed by a Brunauer-Emmett-Teller (BET) analyzer (Belsorp mini II instrument). We also used a Sharif Solar PGE-18 electrochemical impedance spectrometer (EIS) to acquire the electrical parameters of the samples and a Sharif Solar current-voltage (I–V) tracer to find out its photovoltaic performance under an AM1.5 solar light simulator.

3. Results and discussion

We employed XRD analysis to investigate the crystallographic properties of the prepared materials. Fig. 1 shows the X-ray diffraction patterns of the Ni0, Ni1, Ni2 and Ni3 samples. As we can see from the

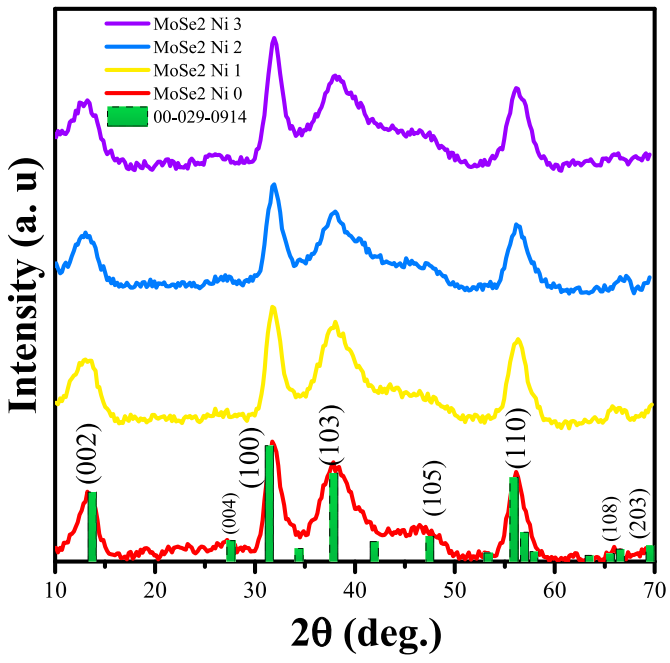

Fig. 1. XRD pattern of $MoSe_2$ counter electrodes synthesized with different Ni concentration.

figure, all the samples demonstrate similar patterns with the least differences between them. This shows that the nickel dopant has not affected the crystalline structure of the $MoSe_2$ layers and thus we do not witness any additional peaks in their XRD patterns. The 2θ diffraction angles in these spectra are 13.56, 27.27, 31.73, 37.84, 47.40, 56.17, 65.97, and 69.51° which respectively demonstrate (002), (004), (100), (103), (105), (110), (108) and (203) crystallographic planes of hexagonal $MoSe_2$ and comply with the standard reference (JCPDS No: 00-029-0914). Using the Debye-Scherrer formula, we can estimate the crystallite sizes of the samples [38]:

$$D = \frac{k\lambda}{\beta\, cos(\theta)}.$$

In this equation, k is the shape constant and equal to 0.89, λ shows the employed X-ray wavelength that in our work is 1.54 Å, β stands for the corresponding full with at half maximum (FWHM) of each peak and θ is the diffraction angle of the X-ray. By averaging the results for different diffraction angles, we can estimate the crystallite sizes of Ni0, Ni1, Ni2, and Ni3 layers to be respectively around 37, 35, 31, and 29 nm. As we can observe in the XRD results, the introduction of the Ni into the $MoSe_2$ lattice have decreased the crystallite sizes of the samples. Although it seems that the Ni doping is negatively affecting the crystallinity of the samples, we expect that its other influences on the physical, electronic and chemical properties of the counter electrode, improve the performance of the DSSCs. Furthermore, the presence of the majority of the peaks in the XRD patterns of these samples shows that there is no preferred orientation. To investigate this, we calculated the texture coefficient from the following equation:

$$TC(hkl) = \left(\frac{I(hkl)/I_0(hkl)}{\frac{1}{n}\sum_n I(hkl)/I_0(hkl)} \right)$$

in which $I(hkl)$ *and* $I_0(hkl)$, are respectively the XRD intensities of the sample and standard references peaks and n is the number of reflections. The texture coefficients of the of Ni0, Ni1, Ni2, and Ni3 samples are summarized in Table 1. In this table, the texture coefficient near 1 shows the conformity with the reference and variation from 1 means that the sample is taking a preferred orientation. From these results, we can conclude that there are no preferred orientations in our prepared counter electrodes and the samples are grown in every direction.

The morphologic properties of the samples were analyzed by electron microscopy. Fig. 2(a–d) displays the FESEM images of the prepared $MoSe_2$ counter electrodes with different concentrations of $NiCl_2$. As we can see from the figure, the surfaces of the layers have a granular morphology with a high amount of porosity. This could be expected from the electrodeposition method to not provide a dense and compact layer. However, these high roughness and porosity are suitable for DSSCs' counter electrode applications [30] and thus we can consider the electrodeposition as a viable and facile method for the preparation of counter electrodes. Moreover, we can see from the images that the surface of the counter electrodes is composed of interconnected nanoparticles with diameters ranging from 50 to 100 nm. Additionally, by increasing the Ni doping, we observe that the number of pores and holes are increased in the counter electrodes. In Fig. 2a which refers to the $MoSe_2$ sample with no Ni doping, we see that the majority of the pores are filled whereas by increasing the Ni content in samples in Ni1, Ni2 and Ni3 the pores are increased and a higher porosity surface is formed. Although, the Ni2 and Ni3 samples possess similar morphologies but their porosity is evidently higher than the Ni0 and Ni1 counter electrodes. We employed the BET analysis to quantitatively investigate the porosities of the samples. Fig. 2e illustrates the adsorption/desorption diagram of the nitrogen in BET analyses for different counter electrodes. The active surface areas of the Ni0, Ni1, Ni2, and Ni3 samples are respectively 49, 57, 86, and 79 cm^2/g which show that the Ni2 sample possesses the highest porosity among our prepared samples.

The dependence of porosity on doping has also been observed before. Gu et al. by fabricating nitrogen-doped porous carbon spheres, improved the porosity in this material, which is essential for electrocatalytic oxygen reduction and enhanced its performance [39]. Chen et al. also by investigating nitrogen doping in carbon nanosheets concluded that nitrogen doping leads to a very large specific surface area (898 $m^2\ g^{-1}$), which increases the catalytic properties of the material [40]. The control of porosity by doping can be justified by the surface formation energy. By changing the Ni doping level, it can be imagined that during the growth, the surface tensions may change in such a way that the surface formation energy is altered. Ni is considered as a defect in the structure of $MoSe_2$. As Fang et al. also point out, during the synthesis, the structure and porosity may change with the formation of defect clusters and defective linkers [41]. The elemental composition of the counter electrodes with different Ni ratios were investigated by the EDS point analysis and illustrated in Fig. 2f. We clearly see from the figure that the counter electrodes are purely made of Se, Mo elements and minor presence of Ni can also be observed. Furthermore, the increase in the concentration of $NiCl_2$ in the preparation step results in the higher amount of Ni elements in the EDS analysis which was expected.

We used the cyclic voltammetry (CV) method for analyzing the electrocatalytic behaviors of the prepared $MoSe_2$:Ni counter electrodes. CV analysis indicates which reactions are taking place on the surface of the counter electrodes and is a powerful tool in determining its properties. For this purpose, we used $MoSe_2$ layers with different Ni ratios as the working electrodes, wire platinum as the counter electrode and the standard Ag/AgCl as the reference electrode and immersed this configuration in a 50-mM LiI, 10-mM I_2, and 0.5-M $LiClO_4$ electrolyte solution. The CV analyses swept a voltage range of −0.5 to 1.5 V with 50 mV/s steps. Fig. 3a, shows the CV results of Ni0, Ni1, Ni2, and Ni3 samples along with the platinum control sample which is the most common counter electrode in DSSCs. We observe in these figures that there are two reduction and two oxidation peaks in every sample which correspond to the redox reactions of $I_3^- + 2e^- \leftrightarrow 3I^-$ and $3I_2 + 2e^- \leftrightarrow 2I_3^-$ [42]. In an illuminated DSSC operation, the dye molecules are oxidized and inject their electron into the photoanode's semiconductor [43]. In other words, I^- gives its additional electron to the dye molecules and oxidizes them. At the same time, the reduced I^- species are changed into I_3^-. The increase in the concentration of I_3^- results in the immigration of these species toward the counter electrode for compensation of their shortage at the surface of the counter electrode due to the diffusion effect. Thus, at the surface of the counter electrode, the I_3^- species, acquire 2 electrons and change into three I^- species according to the $I_3^- + 2e^- \rightarrow 3I^-$ reduction formula. On the other hand, the increase in the concentration of I^- species at counter electrode, increases their diffusion towards the photoanode and forms a cycle which delivers the injected electrons from the counter electrode to the photoanode and completes the circuit. This operation is schematically illustrated in Fig. 3b. Thus, the height of the $I_3^- + 2e^- \rightarrow 3I^-$ reduction peak can demonstrate the counter electrodes' performance. As we can see from Fig. 3a, the height of this half-reaction peak has the highest amount for the Ni2 counter electrode and even surpasses that of the platinum counter electrode. Ni3, Ni1, and Ni0

Table 1
Texture coefficients of different samples for main (hkl) planes of $MoSe_2$ achieved from XRD pattern of different counter electrodes.

(hkl)	Texture coefficient			
	Ni0	Ni1	Ni2	Ni3
(002)	0.991	0.978	0.905	0.906
(004)	1.025	1.125	1.158	1.133
(100)	1.003	1.002	1.089	1.120
(103)	0.990	1.050	0.922	0.916
(110)	0.988	0.944	0.924	0.918

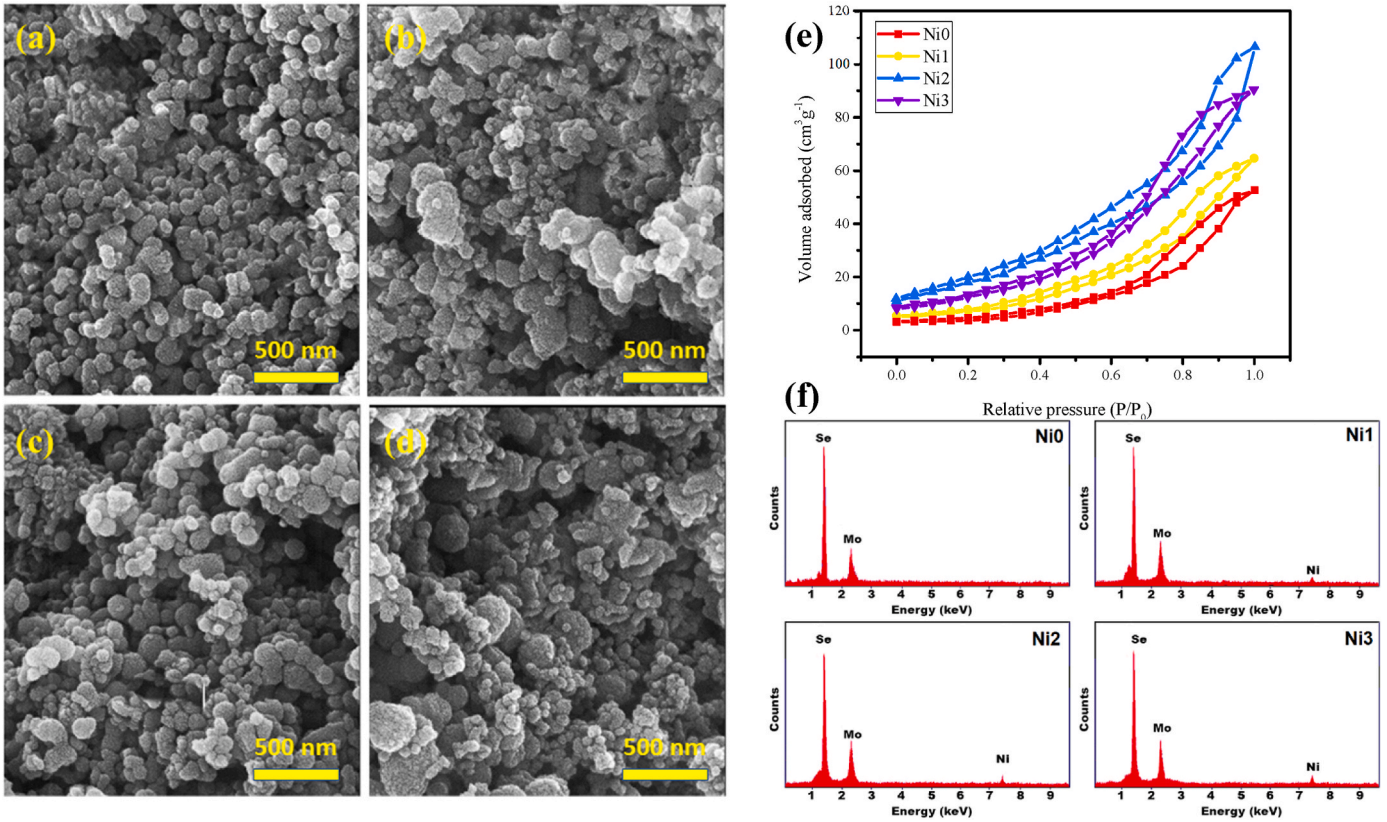

Fig. 2. FESEM images of **(a)** Ni0, **(b)** Ni1, **(c)** Ni2 and **(d)** Ni3 $MoSe_2$ counter electrodes. **(e)** adsorption/desorption of different counter electrode based on relative pressure of N_2 gas (BET analyses). **(f)** point EDS of $MoSe_2$ counter electrodes with various Ni dopant.

samples have respectively the next higher performances. Furthermore, the potential difference between the two oxidation and reduction peaks (E_{PP}) demonstrates the reversibility of the electrode which is another performance factor for counter electrodes and lower E_{pp}s are desirable [44]. According to the CV curves, the Ni2 sample has the lowest E_{pp} among the prepared samples (except the platinum counter electrode). Fig. 3c shows the Tafel polarization diagram for the anodic and cathodic branches of the samples. All the diagrams are calibrated according to their equilibrium potential and thus the equilibrium of the all samples has been occurred at overpotential $\eta = 0$. The intersection between the slope of the linear section of the cathodic branch in the Tafel diagram with the equilibrium axis shows the exchange current density (J_0) [45]. As we can see from the Tafel diagrams, J_0 of the Ni2, platinum, Ni3, Ni1, and Ni0 has the higher values respectively. The higher J_0 is an indicator of better electrocatalytic performance at the counter electrode surface [46]. Therefore, the Ni2 and platinum counter electrodes demonstrate the highest electrocatalytic performances in comparison with the other samples. Furthermore, according to Ref. [47]:

$$J_0 = \frac{RT}{nFR_{ct}}$$

in which R is the universal gas constant, T stands for the absolute temperature, n shows the number of reduction electrons, F is the Faraday constant and R_{ct} shows the charge transfer resistance, we can show that the higher J_0 results in the lower R_{ct}. The lower R_{ct} values indicate easier electron pathways at the surface of the counter electrodes. Therefore, as the R_{ct} of the Ni2 sample confirms its higher electrocatalytic activity. The increased electrocatalytic activity in the Ni2 sample can be corresponded to the results of FESEM and BET analyses. In other word, the increased active surface area in the Ni2 counter electrode also increases the interactions between $MoSe_2$ and electrolyte species which accelerates and increases the electrocatalytic activity.

We employed the EIS analysis to investigate the transport and electrocatalytic performance of $MoSe_2$:Ni electrodes. For this purpose, we used the counter electrode/electrolyte/counter electrode symmetric configuration to eliminate the effects of other DSSC components on the performance of counter electrodes. The EIS analysis was performed in dark condition and frequency range of 0.1–100 kHz with 10 mV perturbation voltage steps. Fig. 3d shows the Nyquist diagrams of the $MoSe_2$ counter electrodes with different ratios of Ni dopant. We observe a single semicircle in the Nyquist diagrams of each sample which is due to the electronic interactions between the electrolyte and counter electrodes [43]. In dark condition, there is no excited electron present to be injected from the configuration into the circuit and the transported electrons are due to the applied potential difference between the two electrodes. These electrons perform transitions from the solid phase to the liquid phase and a charge transfer resistance is created. Therefore, the diameter of the semicircles in the Nyquist diagrams of the EIS analysis demonstrate the R_{ct} of counter electrode/electrolyte interface which their lower values indicate better electrocatalytic activity and transport in the samples [48]. We can calculate the R_{ct} and series resistance (R_s) of the counter electrodes from the Nyquist diagrams in Fig. 3d. The calculated values are summarized in Table 2. As we can see from this table, the R_{ct} values for Ni0, Ni1, Ni2, Ni3, and platinum counter electrodes are respectively 62.66, 48.17, 26.77, 32.47, and 29.96 Ω cm^2 which shows the superiority of Ni2 and platinum counter electrodes in cases of electrocatalytic and transport properties. These results are in correspondence with the CV and Tafel polarization analyses. Moreover, the R_s of Ni0, Ni1, Ni2, Ni3, and platinum counter electrodes are respectively 14.44, 14.10, 11.74, 12.98, and 9.57 Ω cm^2 which shows better conductivity in the platinum counter electrode which is due to the platinum metallic nature.

Thus far, our examination has focused on the physical and electrochemical characteristics of counter electrodes. In order to analyze their

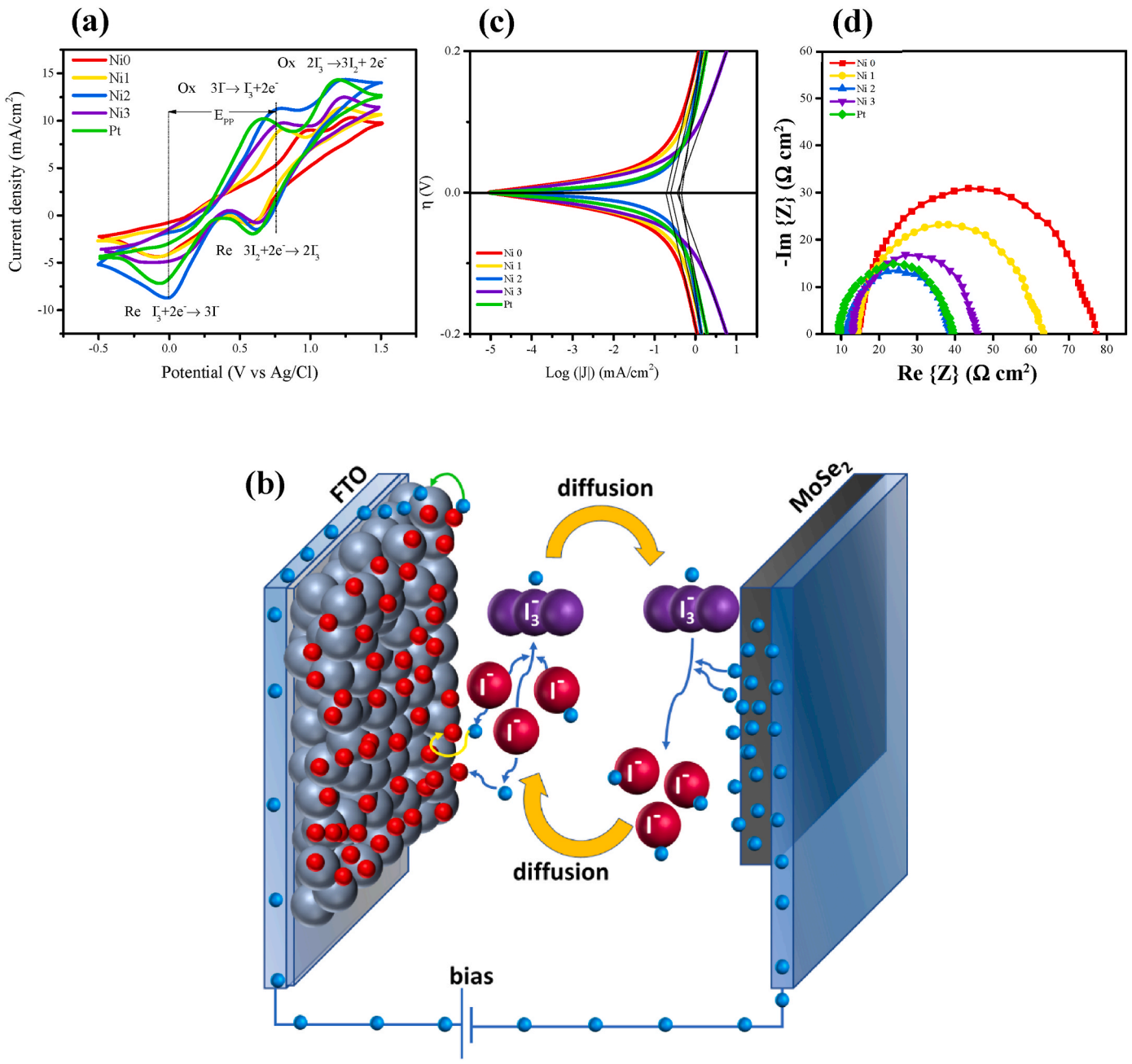

Fig. 3. **(a)** Cyclic voltammetry (CV) of different $MoSe_2$ and Pt counter electrodes. (b) schematic diagram of DSSC performance under illumination. **(c)** Tafel polarization of $MoSe_2$ counter electrodes with different Ni concentrations. **(d)** Nyquist plots for symmetric $MoSe_2$/electrolyte/$MoSe_2$ configuration obtained from EIS measurement.

Table 2
Series resistant (R_s) and charge transport resistance (R_{CT}) of different counter electrodes obtained from Nyquist plots of EIS analyses.

Sample	R_s ($\Omega.cm^2$)	R_{CT} ($\Omega.cm^2$)
Ni 0	14.44	62.66
Ni 1	14.10	48.17
Ni 2	11.74	26.77
Ni 3	12.98	32.47
Pt	9.57	29.96

photovoltaic performances, we acquired their J-V characteristics which are illustrated in Fig. 4a. Furthermore, the photovoltaic parameters of the DSSCs fabricated from Ni0, Ni1, Ni2, Ni3 and platinum counter electrodes are summarized in Table 3. It is clear that the DSSCs fabricated from the Ni2 counter electrode has the highest power conversion efficiency (PCE) of 6.94% while demonstrating an open circuit voltage (V_{OC}) of 688 mV, short circuit current density (J_{SC}) of 16.00 mA/cm^2 and filling factor (FF) of 0.63. the second highest performance DSSC is made with the platinum counter electrode which shows an efficiency of 6.68%. The efficiencies of other samples have lower values of 6.40, 5.87, and 5.63% respectively for Ni3, Ni1, and Ni0 counter electrodes. The higher efficiency of the Ni2 counter electrode is due to its higher J_{SC}. Although the V_{OC} of the DSSC fabricated with platinum counter electrode is 719 mV and is higher than the 688 mV value of the Ni2 DSSC, the higher J_{SC} in the latter sample compensates it and achieves higher efficiency.

V_{OC} of Pt counter electrode is higher than Ni2. However, the efficiency of a solar cell does not depend only on V_{OC} and consists of three

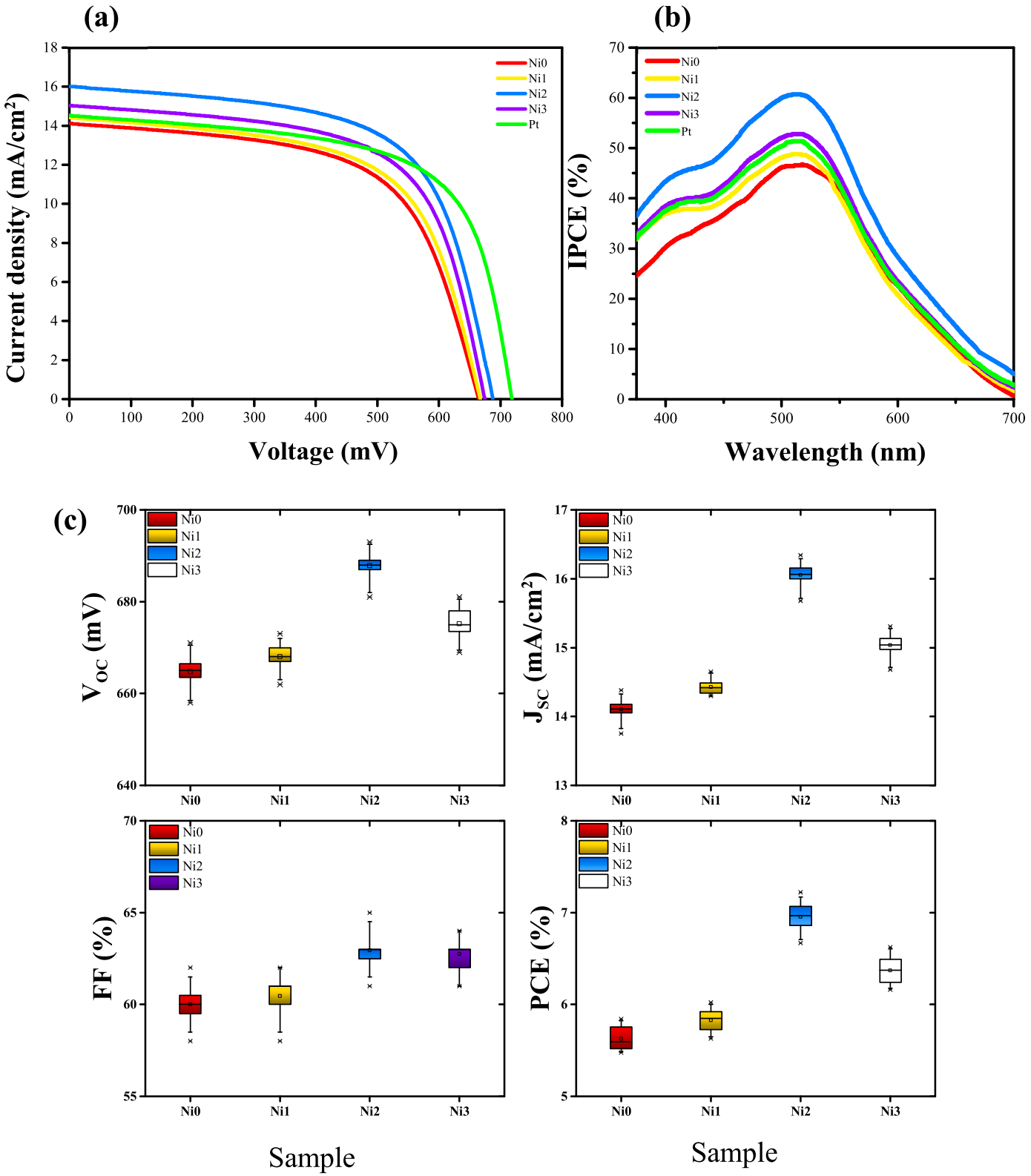

Fig. 4. **(a)** J-V characteristic curves for different DSSCs fabricated by Ni0, Ni1, Ni2 and Ni3 counter electrodes. **(b)** incident to photon current efficiency (IPCE) spectra of different DSSCs assembled by Ni0, Ni1, Ni2 and Ni3 counter electrodes. **(c)** box and whisker diagrams for photovoltaic parameters obtained from 20 DSSCs of each sample.

main components, V_{OC}, J_{SC} and FF, almost each of which originates from separate factors. For example, V_{OC} depends on the difference in quasi-Fermi levels in the semiconductor material and electrolyte redox, while FF is related to the conductivity of the semiconductor [49]. In this way, the tuning of the open circuit voltage is highly dependent on the semiconductor materials. Although, J_{SC} refers to the maximum amount of current that is generated in the solar cell, this current can change drastically by increasing the effective number of dye molecules or the

Table 3
Photovoltaic parameters of different DSSCs assembled by Ni0, Ni1, Ni2, Ni3 and Pt counter electrodes.

Cell	V_{OC} (mV)	J_{SC} (mA/cm^2)	FF (%)	PCE (%)	Maximum IPCE (%)	$J_{SC\text{-}IPCE}$ (mA/cm^2)
Ni 0	665 ± 3.27	14.11 ± 0.13	60 ± 0.9	5.63 ± 0.12	46.7	13.86
Ni 1	667 ± 2.48	14.42 ± 0.09	61 ± 1.1	5.87 ± 0.11	48.8	14.12
Ni 2	688 ± 2.75	16.00 ± 0.15	63 ± 0.8	6.94 ± 0.14	60.7	15.78
Ni 3	675 ± 3.20	15.04 ± 0.15	63 ± 0.9	6.40 ± 0.14	52.8	14.76
Pt	719 ± 3.25	14.52 ± 0.13	64 ± 0.8	6.68 ± 0.11	51.3	14.23

porosity of the materials [38,50]. However, the excessive increase of dye molecules may be destructive and requires an optimal amount. The increase in the electrocatalytic activity of Ni2 counter electrode, as proved in the EIS and CV analyses, provide more current for dye reduction. This leads to an increase in the short circuit current of the Ni2 compared to Pt. Typically, current density has a higher influence on the efficiency because the V_{OC} is mainly determined by the materials bandgap while the J_{SC} is result of many factors that can be altered. The increased J_{SC} in the Ni2 DSSC is due to the role of the counter electrode which accelerates the electrocatalytic processes and improves the charge transport as witnessed in the CV, Tafel, and EIS analyses.

Fig. 4b illustrates the IPCE curves of the fabricated DSSCs. In this figure, we see the incident photon to current efficiency for different wavelengths. Since our DSSCs are prepared using the N719 dye, the absorption peaks of these diagrams are located at 510 nm [51]. We can clearly see that Ni2 DSSC possesses higher quantum efficiency than other samples. The IPCE of the Ni2 DSSC in 450–500 nm wavelengths range is between 45 and 60%. The integral of the IPCE under AM1.5 illumination is equal to the current density of the DSSC which has a good matching with the J_{SC} trend of the J-V analysis. The J_{SC} values were calculated using the IPCE curves and are summarized in Table 3. The results confirm the J-V measurement results and show the highest current for the Ni2 sample.

In order to verify our results and to test their repeatability, the number of 20 DSSCs were fabricated from each sample and their photovoltaic results are illustrated in the form of box and whisker plots in Fig. 4c. This figure shows that our prepared materials and DSSCs possess a high repeatability with minimum error which verifies our results.

Although Pt is accepted as a standard CE for DSSCs, to increase their cost-effectiveness, a huge amount of attention is paid to new CE materials and structures. Carbon black, carbon nanotubes, conductive polymers, sulfides and composite materials are among the various investigated potential replacements for Pt in DSSCs. Lou et al. employed multiwalled carbon nanotube thin films on FTO as CE in DSSCS and achieved efficiencies of up to 4.69% [52]. Nemala et al. could improve the efficiencies to 6.3% by using a solid-state prepared CZTS/CNT composite structure [53]. Gua et al. employed a hydrothermal method to prepared WS_2/MoS_2 composite nanostructure with high porosity and attained efficiencies of around 7.30% [54]. Narudin et al. used ZrO_2 and TTIP binders along with carbon black CEs to achieve around 5.7% efficiencies [7]. Furthermore, Farooq et al. used polyaniline (PANI) doped with sulfuric acid to accomplish 4.54% efficiencies [55]. our work demonstrated a facile low-cost method to achieve around 7% efficiencies which looks quite promising for applications as CE in DSSCs.

As we can clearly see, the $MoSe_2$-based CE demonstrates a good performance and even with higher efficiencies than that of conventional Pt CEs. Since, employing Pt in DSSCs increases the cost of solar energy generation, the new CE can decrease the cost while improving the performance of DSSCs. Furthermore, our proposed fabrication method of the CE, is based on a facile and inexpensive electrochemical technique which can prepare a high-quality layer in short time periods. Moreover, introducing Ni into the $MoSe_2$ structure, provides us with a method to modify the porosity and thus tune the electrocatalytic and electrochemical properties of DSSCs.

4. Conclusion

In summary, we showed that Ni can be efficiently doped into $MoSe_2$ lattice without altering its crystallographic properties while significantly enhancing its electrocatalytic and charge transport characteristics and thus making it a suitable counter electrode for DSSCs. The results of FESEM and BET analyses indicated the improved porosities and higher active surface areas in the Ni2 samples which results in the better electrocatalytic behavior which was confirmed by CV and Tafel experiments. Furthermore, EIS results proved the lower charge transfer resistance in the same sample. The DSSCs fabricated with the optimized Ni2 counter electrode, demonstrated higher efficiencies than any other samples even better than the DSSCs fabricated from conventional platinum counter electrodes. The efficiencies of the DSSCs composed of the optimized Ni-doped $MoSe_2$ and platinum counter electrodes were respectively 6.94 and 6.68%. The higher performance of the Ni2 DSSC is attributed to its increased current density as a result of its improved active surface area, electrocatalytic activity and lower charge transfer resistance.

Author statement

Raed H. Althomali: Project administration, conceptualization, review & editing. **Sulieman Ibraheem Shelash Al-Hawary:** Methodology, original draft, formal analysis. **Anita Gehlot:** Formal analysis, investigation, review & editing. **Maytham T. Qasim:** Formal analysis, investigation, review & editing. **Barno Abdullaeva:** Formal analysis, investigation, review & editing. **I.B. Sapaev:** Validation, data curation, review & editing. **Ibrahim H. Al-Kharsan:** Visualization, data curation, review & editing. **Ali Alsalamy:** Visualization, data curation, review & editing.

Declaration of competing interest

The authors declare that they have no known competing financial interests or personal relationships that could have appeared to influence the work reported in this paper.

Data availability

Data will be made available on request.

References

[1] N.A.A. Malek, N. Alias, A.A. Umar, X. Zhang, X. Li, S.K.M. Saad, N.A. Abdullah, H. Zhang, Z. Weng, Z. Shi, Enhanced charge transfer in atom-thick 2H–WS2 nanosheets' electron transport layers of perovskite solar cells, Solar RRL 4 (2020), 2000260.
[2] S. Mohammadnejad, A. Khalafi, S.M. Ahmadi, Mathematical analysis of total-cross-tied photovoltaic array under partial shading condition and its comparison with other configurations, Sol. Energy 133 (2016) 501–511.
[3] M. Abrari, M. Ahmadi, M. Ghanaatshoar, H.R. Moazami, S.S.H. Davarani, Fabrication of dye-sensitized solar cells based on SnO2/ZnO composite nanostructures: a new facile method using dual anodic dissolution, J. Alloys Compd. 784 (2019) 1036–1046.
[4] H.A. Najafabadi, M. Ahmadi, M. Ghanaatshoar, The influence of radio-frequency sputtered blocking layer on boosting the performance of BaSnO3-based dye-sensitized solar cell, Thin Solid Films 717 (2021), 138346.
[5] H. Esgin, Y. Caglar, M. Caglar, Photovoltaic performance and physical characterization of Cu doped ZnO nanopowders as photoanode for DSSC, J. Alloys Compd. 890 (2022), 161848.
[6] S.A. Ansari, S. Goumri-Said, H.M. Yadav, M. Belarbi, A. Aljaafari, M.B. Kanoun, Directly grown of NiCo2S4 nanoparticles on a conducting substrate towards the high-performance counter electrode in dye-sensitized solar cell: a combined

theoretical and experimental study, Sol. Energy Mater. Sol. Cell. 225 (2021), 111064.
[7] N. Narudin, P. Ekanayake, Y.W. Soon, H. Nakajima, C.M. Lim, Enhanced properties of low-cost carbon black-graphite counter electrode in DSSC by incorporating binders, Sol. Energy 225 (2021) 237–244.
[8] S. Mahato, P. Nandigana, B. Pradhan, B. Subramanian, S.K. Panda, Enhanced efficiency of DSSC by lyophilized tin-doped molybdenum sulfide as counter electrode, J. Alloys Compd. 894 (2022), 162406.
[9] A. Zatirostami, A new electrochemically prepared composite counter electrode for dye-sensitized solar cells, Thin Solid Films 701 (2020), 137926.
[10] N. Alias, A. Ali Umar, N.A.A. Malek, K. Liu, X. Li, N.A. Abdullah, M.M. Rosli, M. Y. Abd Rahman, Z. Shi, X. Zhang, Photoelectrical dynamics uplift in perovskite solar cells by atoms thick 2D TiS2 layer passivation of TiO2 nanograss electron transport layer, ACS Appl. Mater. Interfaces 13 (2021) 3051–3061.
[11] X. Zhang, R. Fan, M. Liu, Y. Cao, P. Sun, Y. Zhang, M. Hao, Y. Zhang, W. Zhang, L. Li, Preparation of CoNi@ CN composites based on metal-organic framework materials as high efficiency counter electrode materials for dye-sensitized solar cells, Sol. Energy 231 (2022) 767–774.
[12] H.R. Moazami, S.S.H. Davarani, M. Abrari, A. Elahi, Electromembrane extraction using a round-headed platinum wire as the inner electrode: a simple and practical way to enhance the performance of extraction, Chromatographia 81 (2018) 1023–1033.
[13] P. Chandra, Applications of 3d-Transition Metals as Pt-free Counter Electrode for Dye-Sensitized Solar Cells Application, Dye-Sensitized Solar Cells, Elsevier, 2022, pp. 213–235.
[14] M. Dissanayake, J. Kumari, G. Senadeera, H. Anwar, Low cost, platinum free counter electrode with reduced graphene oxide and polyaniline embedded SnO2 for efficient dye sensitized solar cells, Sol. Energy 230 (2021) 151–165.
[15] S. Mehmood, S. Suresh, S. Ahmed, M. Alizadeh, N. Abd Rahim, Y. Zhan, Basics of dye sensitized solar cell and use of conductive polymer as counter electrode, Adv. Hybrid Conduct. Polym. Technol. (2021) 327–345. Springer.
[16] S.C. Pradhan, S. Soman, Effect of thickness on charge transfer properties of conductive polymer based PEDOT counter electrodes in DSSC, Results Surf. Interfac. 5 (2021), 100030.
[17] S. Gnanasekar, Q. Van Le, A.N. Grace, Template-free synthesis of Vanadium Nitride Nanopetals (VNNP) as a high performance counter electrode for dye sensitized solar cells, Sol. Energy 213 (2021) 145–153.
[18] S. Gnanasekar, A.N. Grace, Titanium nitride nanoflower buds as Pt-free counter electrodes for dye-sensitized solar cells, ACS Appl. Nano Mater. 4 (2021) 8251–8261.
[19] S. Salleh, M. Rahman, T. Aziz, Dye-sensitized solar cell using nickel sulfide-reduced graphene oxide counter electrode: effect of sulphur content, Inorg. Chem. Commun. 135 (2022), 109086.
[20] Q. Liu, C. Cheng, Facile construction of a polypyrrole–cobalt sulfide counter electrode for low-cost dye-sensitized solar cells, RSC Adv. 11 (2021) 38146–38151.
[21] M. Soltanmohammadi, V. Karimi, S. Alee, M. Abrari, M. Ahmadi, M. Ghanaatshoar, Cu2ZnSnS4 thin film as a counter electrode in zinc stannate-based dye-sensitized solar cells, Semicond. Sci. Technol. 36 (2021), 105008.
[22] J. Theerthagiri, S. Salla, S.J. Lee, G. Maia, J. Madhavan, M.Y. Choi, Dye-Sensitized Solar Cells Configuration with Transition Metal Carbides as Counter Electrode, Counter Electrode for Dye-Sensitized Solar Cells, Jenny Stanford Publishing, 2021, pp. 63–74.
[23] M. Chen, J. Liu, X.-Q. Wang, L.-L. Shao, Z.-Y. Yuan, X. Qian, Y.-N. Wang, A.-X. Ding, Y.-S. Tian, Ultrafine transition metal phosphide nanoparticles semiembedded in nitrogen-doped carbon nanotubes for efficient counter electrode materials in dye-sensitized solar cells, ACS Appl. Energy Mater. (2021).
[24] B. Noorani, S. Ghasemi, S.R. Hosseini, Nanostructured nickel sulfide/graphene oxide-polypyrrole as platinum-free counter electrode for dye-sensitized solar cell, J. Photochem. Photobiol. Chem. 405 (2021), 112966.
[25] M.S. Ahmad, A. Pandey, N. Abd Rahim, N. Aslfattahi, Y.K. Mishra, B. Rashid, R. Saidur, 2-D Mxene flakes as potential replacement for both TCO and Pt layers for Dye-Sensitized Solar cell, Ceram. Int. 47 (2021) 27942–27947.
[26] C. Tamilselvi, P. Duraisamy, N. Subathra, T. Sumathi, R.S. Fredrick, CoSe2/graphene composite: a low-cost, high performance counter electrode for dye sensitized solar cells, J. Phys. Conf. Ser. (2021), 012078. IOP Publishing.
[27] M.I.A. Umar, V. Haris, A.A. Umar, The influence of MoSe2 coated onto Pt film to DSSC performance with the structure TiO2/Dye/LxMoSe2Pt (0≤ x≤ 5), Mater. Lett. 275 (2020), 128076.
[28] N.A. Abd Malek, N. Alias, S.K.M. Saad, N.A. Abdullah, X. Zhang, X. Li, Z. Shi, M. M. Rosli, T.H.T. Abd Aziz, A.A. Umar, Ultra-thin MoS2 nanosheet for electron transport layer of perovskite solar cells, Opt. Mater. 104 (2020), 109933.
[29] A. Zatirostami, Investigating the performance of carbon black/tin selenide composite as the counter electrode in dye sensitized solar cells, J. Electron. Mater. 50 (2021) 1544–1551.
[30] A. Zatirostami, Electro-deposited SnSe on ITO: a low-cost and high-performance counter electrode for DSSCs, J. Alloys Compd. 844 (2020), 156151.
[31] D. Vikraman, S.A. Patil, S. Hussain, N. Mengal, S.H. Jeong, J. Jung, H.J. Park, H.-S. Kim, H.-S. Kim, Construction of dye-sensitized solar cells using wet chemical route synthesized MoSe2 counter electrode, J. Ind. Eng. Chem. 69 (2019) 379–386.
[32] A. Singh, D. Poddar, S. Thakur, R. Jha, Ternary composite based on MoSe2-rGO/polyaniline as an efficient counter electrode catalyst for dye sensitized solar cells, Mater. Chem. Phys. 273 (2021), 125043.
[33] H. Chen, Y. Xie, H. Cui, W. Zhao, X. Zhu, Y. Wang, X. Lü, F. Huang, In situ growth of a MoSe 2/Mo counter electrode for high efficiency dye-sensitized solar cells, Chem. Commun. 50 (2014) 4475–4477.
[34] P. Lynch, U. Khan, A. Harvey, I. Ahmed, J.N. Coleman, Graphene-MoS2 nanosheet composites as electrodes for dye sensitised solar cells, Mater. Res. Express 3 (2016), 035007.
[35] N. Mustaffa, M. Rahman, A. Umar, Dye-sensitized solar cell utilizing silver-reduced graphene oxide film counter electrode: effect of silver content on its performance, Ionics 24 (2018) 3665–3671.
[36] A.R. Tapa, W. Xiang, X. Zhao, Metal chalcogenides (M x E y; E= S, Se, and Te) as counter electrodes for dye–sensitized solar cells: an overview and guidelines, Adv. Energy Sustain. Res. 2 (2021), 2100056.
[37] A. Moradi, M. Abrari, M. Ahmadi, Efficiency enhancement in dye-sensitized solar cells through the decoration of electro-spun TiO 2 nanofibers with Ag nanoparticles, J. Mater. Sci. Mater. Electron. 31 (2020) 16759–16768.
[38] M. Abrari, M. Ghanaatshoar, H.R. Moazami, S.S. Hosseiny Davarani, Synthesis of SnO2 nanoparticles by electrooxidation method and their application in dye-sensitized solar cells: the influence of the counterion, J. Electron. Mater. 48 (2019) 445–453.
[39] D. Gu, R. Ma, Y. Zhou, F. Wang, K. Yan, Q. Liu, J. Wang, Synthesis of nitrogen-doped porous carbon spheres with improved porosity toward the electrocatalytic oxygen reduction, ACS Sustain. Chem. Eng. 5 (2017) 11105–11116.
[40] P. Chen, L.-K. Wang, G. Wang, M.-R. Gao, J. Ge, W.-J. Yuan, Y.-H. Shen, A.-J. Xie, S.-H. Yu, Nitrogen-doped nanoporous carbon nanosheets derived from plant biomass: an efficient catalyst for oxygen reduction reaction, Energy Environ. Sci. 7 (2014) 4095–4103.
[41] Z. Fang, J.P. Dürholt, M. Kauer, W. Zhang, C. Lochenie, B. Jee, B. Albada, N. Metzler-Nolte, A. Poppl, B. Weber, Structural complexity in metal–organic frameworks: simultaneous modification of open metal sites and hierarchical porosity by systematic doping with defective linkers, J. Am. Chem. Soc. 136 (2014) 9627–9636.
[42] D.K. Kumar, S.R. Popuri, S.K. Swami, O.R. Onuoha, J.-W.G. Bos, B. Chen, N. Bennett, H. Upadhyaya, Screen printed tin selenide films used as the counter electrodes in dye sensitized solar cells, Sol. Energy 190 (2019) 28–33.
[43] M. Saeidi, M. Abrari, M. Ahmadi, Fabrication of dye-sensitized solar cell based on mixed tin and zinc oxide nanoparticles, Appl. Phys. A 125 (2019) 1–9.
[44] X. Zheng, J. Deng, N. Wang, D. Deng, W.H. Zhang, X. Bao, C. Li, Podlike N-doped carbon nanotubes encapsulating FeNi alloy nanoparticles: high-performance counter electrode materials for dye-sensitized solar cells, Angew. Chem. Int. Ed. 53 (2014) 7023–7027.
[45] Z. Li, K. Zhao, M. Hao, Z. Zhang, L. Li, Y. Zhang, W. Zhang, A facile hydrothemal synthesis of MoS2@ Co3S4 composites based on metal organic framework compounds as a high-efficiency liquid-state solar cell counter electrode, J. Alloys Compd. 831 (2020), 154910.
[46] R. Kumar, P. Bhargava, Synthesis and characterization of carbon based counter electrode for dye sensitized solar cells (DSSCs) using organic precursor 2-2′ Bipyridine (Bpy) as a carbon material, J. Alloys Compd. 748 (2018) 905–910.
[47] X. Guo, R. Xu, D. Li, Y. Yang, Q. Tian, One-step electrodeposited CoSe2 nano-reticular with high electroconductivity and electrocatalytic as a counter electrode for dye sensitized solar cell, J. Alloys Compd. 831 (2020), 154712.
[48] T. Bai, Y. Xie, J. Hu, C. Zhang, J. Wang, Novel one-dimensional ZnO nanorods synthesized through a two-step post-treatment for efficiency enhancement of dye-sensitized solar cells, J. Alloys Compd. 644 (2015) 350–353.
[49] M. Grätzel, Dye-sensitized solar cells, J. Photochem. Photobiol. C Photochem. Rev. 4 (2003) 145–153.
[50] L. Ellis-Gibbings, V. Johansson, R.B. Walsh, L. Kloo, J.S. Quinton, G.G. Andersson, Formation of N719 dye multilayers on dye sensitized solar cell photoelectrode surfaces investigated by direct determination of element concentration depth profiles, Langmuir 28 (2012) 9431–9439.
[51] M. Abrari, M. Ghanaatshoar, S.S.H. Davarani, H.R. Moazami, I. Kazeminezhad, Synthesis of SnO $$ _ $$ nanoparticles by electrooxidation of tin in quaternary ammonium salt for application in dye-sensitized solar cells, Appl. Phys. A 123 (2017) 326.
[52] X. Luo, J.Y. Ahn, Y.S. Park, J.M. Kim, H.W. Lee, S.H. Kim, Rapid fabrication and photovoltaic performance of Pt-free carbon nanotube counter electrodes of dye-sensitized solar cells, Sol. Energy 150 (2017) 13–19.
[53] S.S. Nemala, K. Mokurala, P. Bhargava, S. Mallick, Cu2ZnSnS4/CNT composites as Pt free counter electrodes for dye sensitized solar cells with improved efficiency, Mater. Today: Proc. 3 (2016) 1808–1814.
[54] F. Guo, B.K. Narukullapati, K.J. Mohammed, U.S. Altimari, A.M. Abed, Z. Yan, N. Ahmad, N.K.A. Dwijendra, R. Sivaraman, A.H. Abdulkadhim, New material for addressing charge transport issue in DSSCs: composite WS2/MoS2 high porosity counter electrodes, Sol. Energy 243 (2022) 62–69.
[55] S. Farooq, A.A. Tahir, U. Krewer, S. Bilal, Efficient photocatalysis through conductive polymer coated FTO counter electrode in platinum free dye sensitized solar cells, Electrochim. Acta 320 (2019), 134544.